Structure of High-Pressure Supercooled and Glassy Water

Riccardo Foffi and Francesco Sciortino[*]

Department of Physics, Sapienza Università di Roma, Piazzale Aldo Moro, 2, 00185 Rome, Italy

We numerically investigate the structure of deep supercooled and glassy water under pressure, covering the range of densities corresponding to the experimentally produced high- and very-high-density amorphous phases. At $T = 188$ K, a continuous increase in density is observed on varying pressure from 2.5 to 13 kbar, with no signs of first-order transitions. Exploiting a recently proposed approach to the analysis of the radial distribution function—based on topological properties of the hydrogen-bond network—we are able to identify well-defined local geometries that involve pairs of molecules separated by multiple hydrogen bonds, specific to the high- and very-high-density structures.

The structure of the different amorphous forms of water, their interconversions and their connection to the liquid state are fascinating topics, which keep capturing the attention of the scientific community [1–5]. One of these amorphous states, the low-density amorphous ice (LDA), can be generated via a multiplicity of processes (vapor deposition [6], hyperquenching [7], heating and decompression of other disordered forms of ice [8]), and it is now well characterized [2,9,10]. LDA has a density $\rho = 0.94$ g cm^{-3} at ambient pressure (P) and temperature $T = 80$ K, and it is characterized by locally tetrahedral structures in which each molecule accepts and donates two hydrogen bonds (HBs), the disordered equivalent of ice I [3]. The results on the high-density forms of amorphous water, for which density and structure seem to be somehow dependent on production process and annealing protocols, are much more controversial. The most recent picture describes two variants of high-density amorphous ice (HDA), called unannealed HDA (uHDA) and expanded HDA (eHDA), characterized by similar densities ρ_{HDA}, 1.15 and 1.13 g cm^{-3}, respectively, along with a third form, the very-high-density amorphous ice (VHDA) with $\rho_{VHDA} = 1.26$ g cm^{-3}. uHDA is the material resulting from compression of ice I_h at 77 K to above GPa pressures [11], while eHDA can be obtained, among other methods, from the decompression of VHDA at 140 K to pressures lower than ≈ 0.1 GPa [8]. Despite their structural similarities, eHDA appears to have a significantly enhanced thermal stability with respect to uHDA [12,13]. VHDA can be prepared either from ice I_h by pressure-induced amorphization above 1.2 GPa at temperatures $130 < T < 150$ K [14] or by annealing uHDA to $T > 160$ K at GPa pressures [15]. More details on the preparation routes of amorphous states can be found in recent reviews [4,16,17].

Recent experimental results show that eHDA can be reversibly transformed into VHDA, suggesting that, despite significant structural differences, eHDA and VHDA might be linked to one another via a continuous thermodynamic path [18]. In other experiments, a seemingly jumplike transition between HDA and VHDA was instead identified [19–21].

Experimental and numerical investigations have established that the most prominent structural difference between the low- and high-density forms of amorphous water is an inward collapse of the second hydration shell, a transformation that mimics the structural changes observed upon compression in the liquid state [22–25]. Less understood are the differences between HDA and VHDA; a further collapse of the second shell has been clearly observed experimentally [23,26,27], but it is not clear if additional novel structural features exist that distinguish VHDA from HDA. Also, a more general question concerns whether, and to what extent, VHDA and HDA actually behave as distinct materials. This Letter focuses exactly on these two points: (a) how can we interpret the structural changes and (b) are eHDA and VHDA separated by a first-order transition? We find that the simulated liquid explores configurations that accurately mimic the structural changes observed experimentally between HDA and VHDA, implying a deep connection between pressure-prepared amorphous ice and deeply supercooled water [25], opposite of conclusions reported in other studies [28,29]. We also find that at such low T the equation of state does not show any unstable region in this density range, consistent with the hypothesis of a continuity of states between eHDA and VHDA. Finally, we characterize the structural crossover from HDA to VHDA by identifying a connection between specific local geometries and topological properties of the HB network, providing a quantitative characterization of what is generically (and possibly improperly) referred to as the collapse of the second neighbor shell.

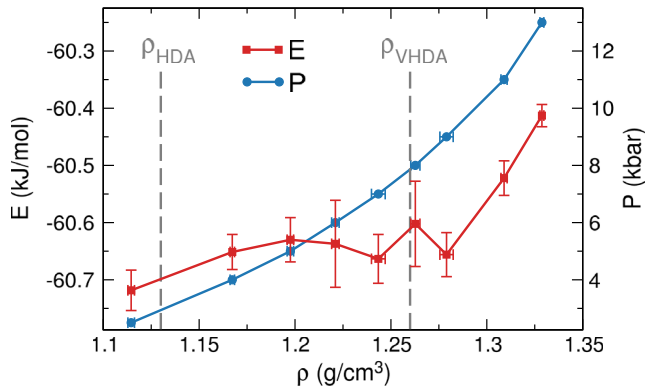A typical experimental procedure to generate HDA and VHDA requires the compression of ice I_h at low T, which

FIG. 1.   Thermodynamics of TIP4P/ice water from MD simulations along the 188 K isotherm. Equation of state (right y axis) and potential energy (per molecule, left y axis) as a function of density. Gray dashed lines show the eHDA and VHDA experimental ρ at 80 K and 1 bar for reference. Error bars are estimated as the variance of the averages over ten distinct time intervals in the production run.
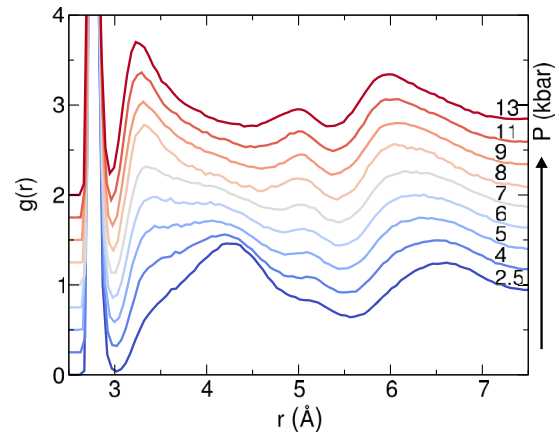

FIG. 2.   Oxygen-oxygen radial distribution function evaluated in the IS along the 188 K isotherm from 2.5 to 13 kbar. The evaluation of the spatial correlations in the IS highlights the evolution of the structural features. Successive $g(r)$ curves are shifted by 0.25 on the vertical axis.

transforms, via a mechanical instability [30], into a disordered material that is later recovered at ambient P. Repeating this process on the computer, while often numerically implemented [25,31–35] requires pressure rates significantly faster than the experimental counterpart, allowing for the possibility that the resulting configurations heavily depend on the protocol. Our numerical approach to generate glass samples exploits the picture of the glass as a quenched liquid. We investigate configurations of high-density liquid water via the TIP4P/Ice potential [36] along a cold ($T = 188$ K) isotherm, right below the model liquid-liquid critical temperature $T_c = 188.6$ K [37], from 2.5 to 13 kbar, corresponding to a density range from 1.1 to 1.3 g cm^{-3}. The results for 2.5 and 4 kbar are reproduced from Ref. [38]. Performing novel numerical simulations longer than 10–25 μs, it is still possible to reach (metastable) equilibrium at this T, eliminating any concern of history dependence and out-of-equilibrium effects. The associated glass structures are provided by the inherent structures (IS), the local energy minima reached via a constant-volume steepest descent procedure that removes vibrational distortions [39]. All the numerical procedures are discussed in detail in the Supplemental Material [40] (which includes Refs. [41–48]).

Figure 1 shows the potential energy (per molecule) E as a function of density (ρ) and the equation of state P vs ρ at $T = 188$ K. In the explored range, $P(\rho)$ has positive concavity and no discontinuities, establishing the absence of any thermodynamic transition between two distinct dense liquid forms along this isotherm. Quite interesting, however, is the density dependence of the potential energy E, which shows a region between 1.12 and 1.25 g cm^{-3} (the typical density values of eHDA and VHDA) in which E weakly depends on ρ, suggesting that the structural changes taking place on increasing pressure have a small

energetic cost. Only beyond ρ_{VHDA}, E grows significantly with ρ.

Figure 2 shows the continuous smooth evolution of the calculated oxygen-oxygen radial distribution function $g(r)$. On increasing P, the concentration of interstitial molecules ($r \approx 3.2$–3.5 Å) increases significantly, while the tetrahedral peak ($r \approx 4.4$ Å) is suppressed. Two additional features characterize the evolution: the development of a novel peak at $r \approx 5$ Å and the intensity crossover from $r \approx 6.7$ to ≈ 6 Å. The corresponding evolution of the structure factor [49] is reported in the Supplemental Material [40].

Before interpreting the structural features, we validate the numerical results comparing the structure of the glasses generated by quenching equilibrium liquid configurations with available experimental data of eHDA and VHDA structures from Mariedahl *et al.* [23] and Bowron *et al.* [9]. To do so, we quench configurations equilibrated at $T = 188$ K and different P to $T = 80$ K and ambient pressure—the same T and P in Refs. [9,23]. Following a short MD simulation, the density and the vibrational and rotational degrees of freedom adjust to $T = 188$ K and $P = 1$ bar. More details can be found in the Supplemental Material [40]. Since classical calculations neglect the quantum delocalization of the atoms [50,51], the height of the first peak of $g(r)$ is usually overestimated. To include in an effective way the quantum broadening of O—O distances (as well as any possible broadening due to the experimental procedures) we have convoluted the numerical $g(r)$ with a Gaussian of variance $\sigma_B^2 = 7.1 \times 10^{-3}$ Å^2, a value obtained by matching the heights of the first peak in the numerical $g(r)$ to the experimental values. This value is consistent with the broadening observed between path-integral and classical
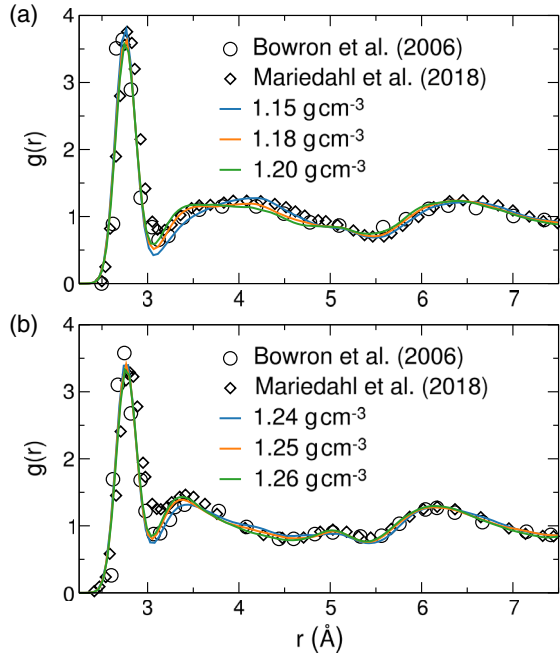
FIG. 3. Comparison between experimental (symbols) and numerical (lines) $g(r)$ in (a) eHDA and (b) VHDA at $T = 80$ K and $P = 1$ bar [9,23]. The densities indicated in the label refer to the values at ambient pressure.
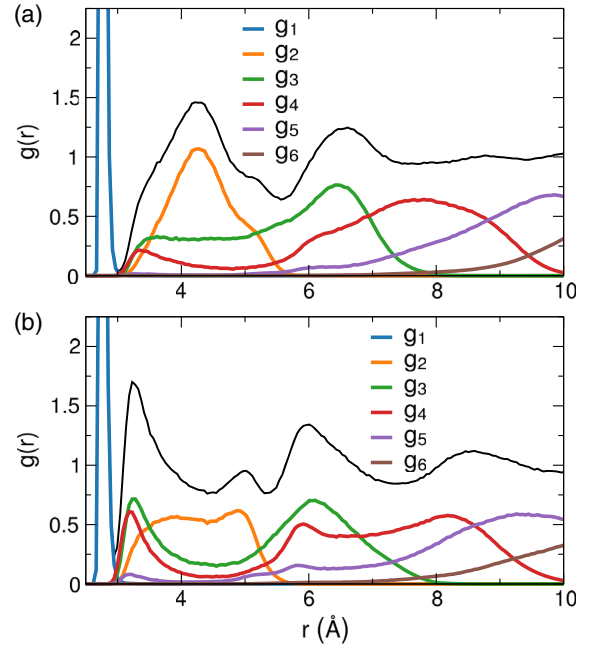

FIG. 4. Radial distribution function of water (evaluated in the IS) at 188 K and P (a) 2.5 kbar and (b) 13 kbar separated in their g_D contributions ($1 \leq D \leq 6$) from pairs of molecules at chemical distance D. The black line is the sum over all $g_D(r)$, equal to the total $g(r)$ [Eq. (1)].

simulations of the same model [51]. Note that the implemented broadening becomes irrelevant when $r \gg \sigma_B$ (Fig. S8 reports the comparison without the correction [40]). We compare the experimental data (which display some differences, possibly due to different preparation histories) to numerical $g(r)$'s with ρ's comparable to experimental values typical of HDA and VHDA. Figure 3 shows that both eHDA and VHDA radial features are rather faithfully reproduced by TIP4P-ice. The quality of the comparison enforces our confidence in the TIP4P-ice model to properly describe the local geometries responsible for the structural signatures observed experimentally, as detailed in the following analysis.

To gain a better insight into the structural changes on going from eHDA to VHDA, we adopt a methodology recently proposed to investigate the liquid-liquid phase transition [38]. We separate the contributions to the $g(r)$ originating from pairs of molecules with "chemical distance" D, where D is defined as the minimum number of HBs connecting the two molecules along the HB network. An analysis based on the HB network topology depends crucially on the ability to properly identify HBs. In TIP4P-ice, HBs can be accurately identified at all pressures (Figs. S9–S11 [40]) adopting the Luzar-Chandler definition [52]. Furthermore, at all explored densities, more than 99.5% of the H atoms are involved in HBs, indicating that practically all molecules donate two hydrogens for bonding (Fig. S12).

We connect structure and network topology by writing

$$g(r) = \sum_{D} g_D(r), \tag{1}$$

where $g_D(r)$ is the radial distribution function evaluated among only pairs of molecules at chemical distance D. The effects of this decomposition are shown for the lowest and highest studied P (2.5 and 13 kbar) in Fig. 4. The partitioning reveals precise relationships between spatial and topological features, providing insight into the structural evolution that occurs upon compression and thus facilitating a classification of molecule pairs into distinct groups. First, we observe well-defined peaks at $r \leq 3.5$ Å for $D = 3$–5, clarifying that interstitial molecules, despite their close real-space distance, reaching down to $r \approx 3$ Å, are separated by three or more HBs. The growth in the number of interstitial molecules (a phenomenon that characterizes the transition from the low- to the high-density liquid [38]) is significantly enhanced on going from HDA- to VHDA-like densities. Figure 4 also shows that the peak at $r \approx 5$ Å can be associated with molecules separated only by two HBs ($D = 2$) and that the peak at $r \approx 6$ Å originates from pairs with chemical distance $D = 4$. Indeed, while $D = 3$ provides a major contribution to $g(r \approx 6$ Å$)$, only in $D = 4$ a new peak arises, continuously growing upon compression from high to very high densities.
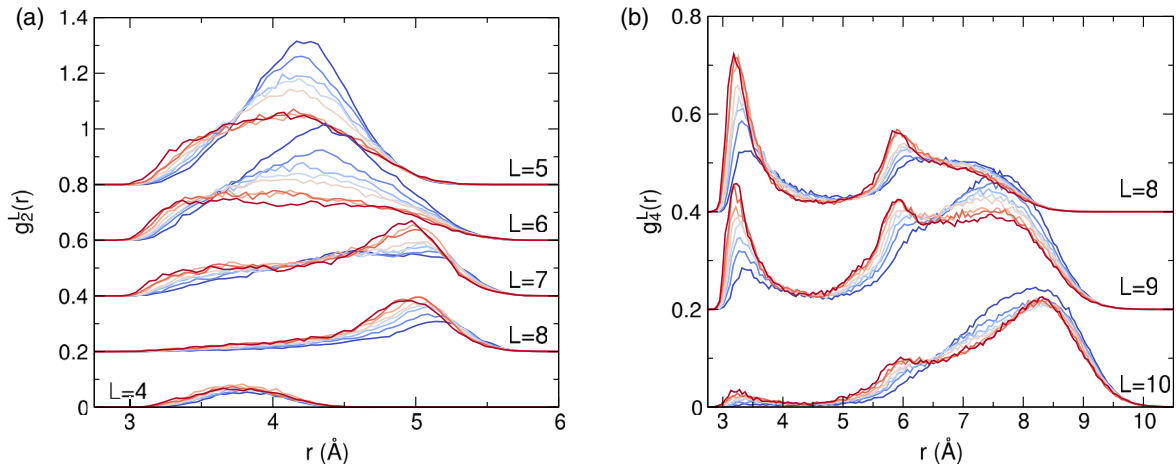
FIG. 5. Contribution to the radial distribution function from pairs of molecules at (a) $D = 2$ and (b) $D = 4$, separated according to the ring length L, along the $T = 188$ K isotherm. Colors from red to blue indicate increasing pressure from 2.5 to 13 kbar. Note that for $D = 2$ and $L = 7$ and 8, a clear peak progressively grows at $r \approx 5$ Å. Also note that, for $D = 4$, beside the growth at the interstitial distance $r \approx 3.2$ Å a further peak appears at $r \approx 6$ Å, most clearly for $L = 8$ and $L = 9$.

Finally, $g_2(r)$ shows a complete disappearance of the tetrahedral peak at 4.4 Å—the landmark of the low-density liquid, still quite intense in the high-density liquid at coexistence [38]—which progressively transforms into a broad featureless distribution, indicating a significant broadening of the OÔO angle of H-bonded triplets of molecules.

To pin down the local geometries responsible for the peaks, $g_D(r)$ can be further decomposed into contributions from "rings" of different length [38]. To each pair of molecules contributing to $g(r)$, we now associate, in addition to the spatial distance r and chemical distance D, also a ring length L. The ring is selected by joining the two shortest nonintersecting HB paths connecting the selected pair (see also Fig. S15 for an example [40]). Then each g_D can be written as

$$g_D(r) = \sum_L g_D^L(r), \qquad (2)$$

where g_D^L indicates the contribution to $g(r)$ from all pairs of molecules with chemical distance D and ring length L.

This analysis applied to $g_2(r)$, detailed in Fig. 5(a), reveals that the peak at $r \approx 5$ Å originates from pairs at $D = 2$, which are part of rings of length $L = 7$ and 8. An example of the corresponding molecular arrangement is shown in Fig. 6(a). Since the length of a HB is strongly constrained around ≈ 2.8 Å, these types of configurations at $D = 2$ are associated with typical OÔO angles of about 135°. Such large angles (compared to the tetrahedral one) propagate in the HB network, promoting the formation of $L \geq 7$ rings. The same strategy [Eq. (2)] also allows us to associate the peak at ≈ 6 Å to pairs at $D = 4$ for different values of L; the decomposition of $g_4(r)$ is reported in

Fig. 5(b). Pairs at $r \approx 6$ Å are found in rings with a squarelike segment such that they are almost collinear with a third molecule, H bonded to only one of them, as seen in Fig. 6(b). Pairs with $D = 4$ and $L = 8$ also provide a major contribution to the interstitial region with a crystal-clear peak shifting from 3.5 to 3.2 Å with increasing P,
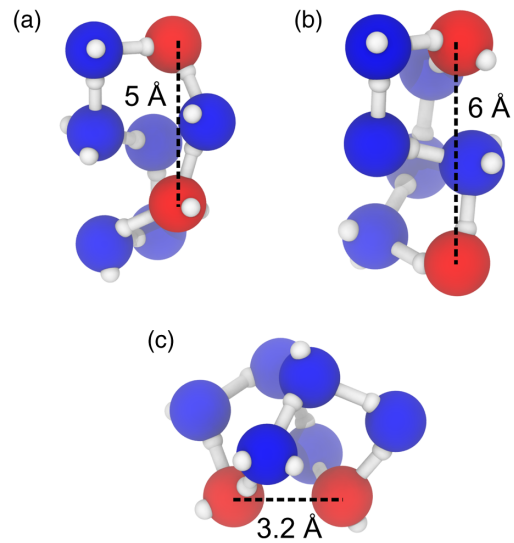

FIG. 6. Cartoon representation of the three local geometries that characterize water under high pressure: (a) pairs at $D = 2$ and $L = 8$ (D2L8) and (b),(c) pairs with $D = 4$ and $L = 8$ (D4L8). D2L8 pairs are separated by a single molecule with a wide angle between the two HBs and contribute to the $g(r)$ peak at $r \approx 5$ Å. D4L8 pairs contribute to the peaks at $r \approx 6$ and $r \approx 3.2$ Å. In the first case (b), the pair is almost collinear with a third molecule H bonded to only one of them; in the latter (c), the folding back of the ring allows the pair to get very close despite the large chemical distance.

signaling a drastic network restructuring linked to the interpenetration of bond-coordination shells. An example of this local geometry is provided in Fig. 6(c). Videos S1–S3 included in the Supplemental Material [40] facilitate the visualization of these geometric arrangements.

In summary, by exploring with lengthy simulations the high-density liquid in TIP4P-ice at $T = 188$ K (below the model liquid-liquid T_c), we have demonstrated that the liquid structure continuously evolves from eHDA to VHDA, supporting an interpretation of water high-density glasses based on thermodynamic continuity. Both eHDA and VHDA can be seen as the kinetically arrested counterparts of a single high-density liquid, which is mirrored by eHDA close to the liquid-liquid transition pressure and progressively more by VHDA as P is increased. Together with the experimentally established connection between the low-density liquid and LDA [53,54], our finding reinforces the hypothesis, based on the liquid-liquid critical point idea [31,55,56], that LDA and HDA-VHDA are the amorphous phases associated with the low- and high-density liquids, with no need to invoke a derailed crystallization pathway [28,29].

We have also identified the geometrical origin of the structural changes taking place on going from eHDA to VHDA: (i) interstitial molecules arising from long rings with a "folded" structure, bringing molecules separated by three or four HBs close by in space, (ii) progressive distortion of the OÔO angle, favoring larger ring sizes (and responsible for the peak at $r \approx 5$ Å), and (iii) specific structural motifs in rings of length $L \geq 8$ such that molecules separated by four HBs remain at distance ≈ 6 Å.

---

*Corresponding author.
francesco.sciortino@uniroma1.it

[1] O. Mishima and H. E. Stanley, Nature (London) **396,** 329 (1998).

[2] P. G. Debenedetti, J. Phys. Condens. Matter **15,** R1669 (2003).

[3] K. Amann-Winkel, R. Böhmer, F. Fujara, C. Gainaru, B. Geil, and T. Loerting, Rev. Mod. Phys. **88,** 011002 (2016).

[4] P. H. Handle, T. Loerting, and F. Sciortino, Proc. Natl. Acad. Sci. U.S.A. **114,** 13336 (2017).

[5] H. Tanaka, J. Chem. Phys. **153,** 130901 (2020).

[6] E. F. Burton and W. F. Oliver, Proc. R. Soc. A **153,** 166 (1935).

[7] E. Mayer, J. Appl. Phys. **58,** 663 (1985).

[8] K. Winkel, M. S. Elsaesser, E. Mayer, and T. Loerting, J. Chem. Phys. **128,** 044510 (2008).

[9] D. T. Bowron, J. L. Finney, A. Hallbrucker, I. Kohl, T. Loerting, E. Mayer, and A. K. Soper, J. Chem. Phys. **125,** 194502 (2006).

[10] P. H. Handle and T. Loerting, J. Chem. Phys. **148,** 124508 (2018).

[11] O. Mishima, L. D. Calvert, and E. Whalley, Nature (London) **310,** 393 (1984).

[12] K. Amann-Winkel, C. Gainaru, P. H. Handle, M. Seidl, H. Nelson, R. Bohmer, and T. Loerting, Proc. Natl. Acad. Sci. U.S.A. **110,** 17720 (2013).

[13] V. Fuentes-Landete, L. J. Plaga, M. Keppler, R. Böhmer, and T. Loerting, Phys. Rev. X **9,** 011015 (2019).

[14] O. Mishima, Nature (London) **384,** 546 (1996).

[15] T. Loerting, C. Salzmann, I. Kohl, E. Mayer, and A. Hallbrucker, Phys. Chem. Chem. Phys. **3,** 5355 (2001).

[16] T. Loerting, K. Winkel, M. Seidl, M. Bauer, C. Mitterdorfer, P. H. Handle, C. G. Salzmann, E. Mayer, J. L. Finney, and D. T. Bowron, Phys. Chem. Chem. Phys. **13,** 8783 (2011).

[17] J. L. Finney, *Water: A Very Short Introduction*, 1st ed., Very Short Introductions No. 440 (Oxford University Press, Oxford, United Kingdom, 2015).

[18] P. H. Handle and T. Loerting, J. Chem. Phys. **148,** 124509 (2018).

[19] T. Loerting, C. G. Salzmann, K. Winkel, and E. Mayer, Phys. Chem. Chem. Phys. **8,** 2810 (2006).

[20] T. Loerting, W. Schustereder, K. Winkel, C. G. Salzmann, I. Kohl, and E. Mayer, Phys. Rev. Lett. **96,** 025702 (2006).

[21] C. G. Salzmann, T. Loerting, S. Klotz, P. W. Mirwald, A. Hallbrucker, and E. Mayer, Phys. Chem. Chem. Phys. **8,** 386 (2006).

[22] A. K. Soper and M. A. Ricci, Phys. Rev. Lett. **84,** 2881 (2000).

[23] D. Mariedahl, F. Perakis, A. Späh, H. Pathak, K. H. Kim, G. Camisasca, D. Schlesinger, C. Benmore, L. G. M. Pettersson, A. Nilsson, and K. Amann-Winkel, J. Phys. Chem. B **122,** 7616 (2018).

[24] H. Tanaka, H. Tong, R. Shi, and J. Russo, Nat. Rev. Phys. **1,** 333 (2019).

[25] F. Martelli, F. Leoni, F. Sciortino, and J. Russo, J. Chem. Phys. **153,** 104503 (2020).

[26] J. L. Finney, D. T. Bowron, A. K. Soper, T. Loerting, E. Mayer, and A. Hallbrucker, Phys. Rev. Lett. **89,** 205503 (2002).

[27] K. Amann-Winkel, D. T. Bowron, and T. Loerting, Mol. Phys. **117,** 3207 (2019).

[28] J. J. Shephard, S. Ling, G. C. Sosso, A. Michaelides, B. Slater, and C. G. Salzmann, J. Phys. Chem. Lett. **8,** 1645 (2017).

[29] C. A. Tulk, J. J. Molaison, A. R. Makhluf, C. E. Manning, and D. D. Klug, Nature (London) **569,** 542 (2019).

[30] J. S. Tse, D. D. Klug, C. A. Tulk, I. Swainson, E. C. Svensson, C.-K. Loong, V. Shpakov, V. R. Belosludov, R. V. Belosludov, and Y. Kawazoe, Nature (London) **400,** 647 (1999).

[31] P. H. Poole, F. Sciortino, U. Essmann, and H. E. Stanley, Nature (London) **360,** 324 (1992).

[32] N. Giovambattista, H. E. Stanley, and F. Sciortino, Phys. Rev. E **72,** 031510 (2005).

[33] N. Giovambattista, H. E. Stanley, and F. Sciortino, Phys. Rev. Lett. **94,** 107803 (2005).

[34] R. Martoňák, D. Donadio, and M. Parrinello, J. Chem. Phys. **122,** 134501 (2005).

[35] P. H. Handle, F. Sciortino, and N. Giovambattista, J. Chem. Phys. **150**, 244506 (2019).

[36] J. L. F. Abascal, E. Sanz, R. García Fernández, and C. Vega, J. Chem. Phys. **122**, 234511 (2005).

[37] P. G. Debenedetti, F. Sciortino, and G. H. Zerze, Science **369**, 289 (2020).

[38] R. Foffi, J. Russo, and F. Sciortino, J. Chem. Phys. **154**, 184506 (2021).

[39] F. H. Stillinger, *Energy Landscapes, Inherent Structures, and Condensed-Matter Phenomena* (Princeton University Press, Princeton, New Jersey, 2015).

[40] See Supplemental Material at http://link.aps.org/supplemental/10.1103/PhysRevLett.127.175502 for additional details on numerical methods and results, which includes Refs. [41–48].

[41] M. J. Abraham, T. Murtola, R. Schulz, S. Páll, J. C. Smith, B. Hess, and E. Lindahl, SoftwareX **1–2**, 19 (2015).

[42] D. Frenkel and B. Smit, *Understanding Molecular Simulation from Algorithms to Applications* (Academic Press, San Diego, 2002).

[43] M. Parrinello and A. Rahman, J. Appl. Phys. **52**, 7182 (1981).

[44] B. Hess, H. Bekker, H. J. C. Berendsen, and J. G. E. M. Fraaije, J. Comput. Chem. **18**, 1463 (1997).

[45] M. P. Allen and D. J. Tildesley, *Computer Simulation of Liquids*, 2nd ed. (Oxford University Press, Oxford, 2017).

[46] H. J. C. Berendsen, J. P. M. Postma, W. F. van Gunsteren, A. DiNola, and J. R. Haak, J. Chem. Phys. **81**, 3684 (1984).

[47] R. Kumar, J. R. Schmidt, and J. L. Skinner, J. Chem. Phys. **126**, 204107 (2007).

[48] S. Saito, B. Bagchi, and I. Ohmine, J. Chem. Phys. **149**, 124504 (2018).

[49] J.-P. Hansen and I. R. McDonald, *Theory of Simple Liquids: With Applications of Soft Matter* (Elsevier, Academic Press, Amsterdam, 2013).

[50] C. P. Herrero and R. Ramírez, Phys. Rev. B **84**, 224112 (2011).

[51] C. P. Herrero and R. Ramírez, J. Chem. Phys. **137**, 104505 (2012).

[52] A. Luzar and D. Chandler, Nature (London) **379**, 55 (1996).

[53] L. Kringle, W. A. Thornley, B. D. Kay, and G. A. Kimmel, Science **369**, 1490 (2020).

[54] L. Kringle, W. A. Thornley, B. D. Kay, and G. A. Kimmel, Proc. Natl. Acad. Sci. U.S.A. **118**, e2022884118 (2021).

[55] J. C. Palmer, P. H. Poole, F. Sciortino, and P. G. Debenedetti, Chem. Rev. **118**, 9129 (2018).

[56] K. H. Kim *et al.*, Science **370**, 978 (2020).